

RSC Advances



This is an *Accepted Manuscript*, which has been through the Royal Society of Chemistry peer review process and has been accepted for publication.

Accepted Manuscripts are published online shortly after acceptance, before technical editing, formatting and proof reading. Using this free service, authors can make their results available to the community, in citable form, before we publish the edited article. This *Accepted Manuscript* will be replaced by the edited, formatted and paginated article as soon as this is available.

You can find more information about *Accepted Manuscripts* in the [Information for Authors](#).

Please note that technical editing may introduce minor changes to the text and/or graphics, which may alter content. The journal's standard [Terms & Conditions](#) and the [Ethical guidelines](#) still apply. In no event shall the Royal Society of Chemistry be held responsible for any errors or omissions in this *Accepted Manuscript* or any consequences arising from the use of any information it contains.

Cite this: DOI: 10.1039/c0xx00000x

www.rsc.org/xxxxxx

ARTICLE TYPE

MnO₂ nanoflakes grown on 3D graphite network for enhanced electrocapacitive performance

Xiuxia Sun,^a Huanjing Wang,^a Zhibin Lei,^{a*} Zonghuai Liu^a and Lingling Wei^{b*}*Received (in XXX, XXX) Xth XXXXXXXXXX 20XX, Accepted Xth XXXXXXXXXX 20XX*

DOI: 10.1039/b000000x

The free-standing 3D graphite (3DG) with interconnected porous network and highly conductive backbone was prepared by a chemical vapor deposition technique with Ni foam as sacrificial template and styrene as carbon precursor. The 3D graphite network serves as an excellent scaffold to grow MnO₂ nanoflakes through a hydrothermal reaction between 3DG and KMnO₄ aqueous solution. The interconnected and conductive 3D graphite network offer a pathway for fast electron and ion transport, while the MnO₂ nanoflakes that intimately emanate from the backbone surface of 3DG minimize the interfacial contact resistance between 3DG and MnO₂, favouring the effective electron transport from 3DG skeleton to MnO₂ nanoflakes. As a result, the 3DG-MnO₂ composite electrode with 13% MnO₂ nanoflakes exhibited a specific capacitance of 210 F g⁻¹ at constant discharge current density of 2.0 A g⁻¹ and still remains 202 F g⁻¹ at high current density of 15 A g⁻¹. Moreover, a good capacitance retention of 75% and an outstanding Coulombic efficiency of 97.8% were achieved after 4000 cycles of galvanostatic charge-discharge. These superior capacitive properties make 3DG-MnO₂ composite one of promising electrode for electrochemical energy storage..

Introduction

Supercapacitors are of great interests as energy storage devices because of their unique properties including high power density, fast charge-discharge rate, excellent cycling performance and low maintenance cost.¹⁻⁵ These advantages make supercapacitor one of the most attractive power devices that have extensive applications in mobile electronics, hybrid electric vehicles and large industrial equipment.^{4,6,7} The carbon-based supercapacitor store energy through fast ion adsorption on the electrode surface.^{5,8} Whereas, the conducting polymers and metal oxides accumulate charges by reversible electrochemical redox reactions at the electrode/electrolyte interface.⁹ Due to the involved electrochemical Faradic redox reaction, pseudocapacitors usually deliver a much high capacitance than electric double-layer capacitor (EDLC). Among various pseudocapacitive materials, MnO₂ has received great attention because of its high theoretical capacitance, low cost and environmental compatibility properties.¹⁰⁻¹³ However, MnO₂-based electrode usually suffers from the poor cycling stability, low electrical conductivity and the large volume expand/shrinkage during charging-discharging process,^{14,15} which greatly preclude their practical applications in supercapacitor.

Given that MnO₂ contributes to the capacitance through a fast surface Faradic redox reaction, MnO₂ electrode with a large electrochemically active surface area is expected to offer a much shortened ion diffusion pathway for effective electrolyte penetration, and thus to maximize the Faradic redox reaction.^{16,17} On the other hand, the rate performance of MnO₂ electrode also

strongly depends on how fast the electron and ion can transport in the interior of electrode. A common strategy to promote the electron transport is to incorporate the pseudocapacitive MnO₂ electrode onto a highly conductive and electrochemically stable support with a large ion-accessible surface area.¹⁸⁻²⁰ Having the excellent electrical conductivity and possessing an unique two-dimensional planar nanostructure, graphene holds great promise as attractive matrixes to accommodate various pseudocapacitive materials for electrochemical energy storage.²¹⁻²⁵ The usual method for preparing MnO₂-graphene composite electrode involves the solution-based electrostatic self-assembly or the physical combining of MnO₂ with the chemically reduced graphene oxides (RGO).²⁶⁻²⁹ In such system, the active MnO₂ nanostructures are mostly in poor contact with the RGO matrixes. The large interfacial resistance largely affects the effective charge transfer from graphene matrix to the active MnO₂. Moreover, the relatively low electronic conductivity of RGO due to the substantial number of residual oxygen functional groups, and the densely packed graphene layers which block the access of electrolyte make RGO not a preferable matrix to accommodate the pseudocapacitive MnO₂ component.

In contrast, three-dimensional graphene with interconnected networks show many attractive and competitive advantages as compared with RGO with respect to its excellent electronic conductivity, three-dimensional porous structure and good mechanical flexibility.^{23,25,30-38} Herein, we reported the capacitive performance of MnO₂ nanoflakes that were grown on the highly conductive three-dimensional graphite network (3DG). The 3D graphite network was prepared by a chemical vapor deposition

with commercially available Ni foam as sacrificial template and the styrene as carbon precursor. The hydrothermal reaction between 3DG and aqueous KMnO_4 allows for the uniform growth of MnO_2 nanoflakes on the surface of 3DG backbone to form a hybrid nanostructure (3DG- MnO_2). The 3DG with seamlessly interconnected porous network serves as excellent scaffold to enhance the electron and ion transport, while the intimate junction between 3DG backbone and MnO_2 minimizes the interfacial contact resistance and greatly promotes the electron migration from 3DG network to MnO_2 . Moreover, the uniform MnO_2 nanoflakes offer a large electrochemically active surface area for electrolyte penetration. As a result, the composite electrode delivers a high specific capacitance of 210 F g^{-1} at 2.0 A g^{-1} and remains a high capacitance of 202 F g^{-1} at 15 A g^{-1} . Importantly, a good capacitance retention of 75% and an outstanding Coulombic efficiency of 97.8% were also achieved even after 4000 cycles of galvanostatic charge-discharge.

Experimental

Sample preparation

The 3D graphite network were prepared by a chemical vapor deposition method with 3D Ni foam as sacrificial template and styrene as carbon precursor. Prior to the CVD process, the Ni foam (purchased from Changsha Iyrun new material Co. Ltd in China with a density of 380 g m^{-2} and thickness of 1.5 mm,) were cut into $1.2 \text{ cm} \times 1.5 \text{ cm}$ sheets and then were pressed into 0.6 mm thick. These Ni pieces were sequentially treated with 1.0 mol L^{-1} HCl for 10 min, and rinsed with acetone and deionized water, respectively. The treated Ni foam pieces were loaded in the quartz boat, which was placed in the center of quartz tube heated by a program-controlled electric furnace. After the temperature of the furnace was raised to $900 \text{ }^\circ\text{C}$ with a ramp rate of $10 \text{ }^\circ\text{C min}^{-1}$ under Ar gas flow, the Ar gas saturated with styrene (50 sccm) was introduced in the furnace for 60 min. The Ni foam covered with graphene was naturally cooled to room temperature.

To preserve the structural integration of 3D graphite network, the 3DG/Ni foam was firstly immersing in poly(methyl methacrylate) (PMMA, average molecular weight of 996000) solution (4.5% PMMA dissolved in anisole) for 10 min. The 3DG/Ni foam loaded with PMMA was then baked at $160 \text{ }^\circ\text{C}$ for 30 min to solidify the composite, which was subsequently immersed into 6.0 mol L^{-1} HCl solution for 24 h to completely remove Ni foam. Finally, the PMMA coated 3D graphene was dissolved by immersing the composite in hot acetone for 2 h, followed by rinsed with copious water and ethanol and dried at $80 \text{ }^\circ\text{C}$. Growth of MnO_2 nanoflake on 3D graphite was achieved by the following stoichiometric reaction between 3DG and KMnO_4 :^{26, 39}



In a typical procedure, 3DG was placed in an autoclave with 40 mL water containing given amount of KMnO_4 . The hydrothermal reaction was conducted at $140 \text{ }^\circ\text{C}$ for 3 h. The final product was collected by rinsing with copious water and drying at $80 \text{ }^\circ\text{C}$. The mass content of MnO_2 in the 3DG- MnO_2 composite was calculated by measuring the weight of sample before and after

hydrothermal reaction.

Characterization

X-ray diffraction (XRD) measurements were carried out using a D/Max-3c X-ray diffractometer with $\text{Cu K}\alpha$ ($\lambda=0.154 \text{ nm}$), using an operation voltage and current of 40 kV and 30 mA, respectively. The morphology of the samples was observed by a field-emission scanning electron microscopy (FESEM) on FEI Quanta 600F equipped with an energy-dispersed X-ray spectrometer (EDX) analyzing system. The microstructure of the samples was examined on a JEOL-2100F HRTEM at an acceleration voltage of 200 kV. X-ray photoelectron spectroscopy (XPS) spectra were collected on an AXIS ULTRA spectrometer (Kratos Analytical) using a monochromatized Al $\text{K}\alpha$ X-ray source (1486.71 eV). Raman spectra were measured on a Renishaw inVia Raman microscope with an excitation wavelength of 514.5 nm. The electrical conductivity of the graphite network was measured by a four-point probe technique. The sample was pressed into a thin disk under a pressure of 15 Mpa.

Electrochemical measurements

The electrochemical performance of the electrode materials was characterized by cyclic voltammetry (CV), galvanostatic charge-discharge and electrochemical impedance spectroscopy (EIS) on a CHI 660D (Chenhua, Shanghai) electrochemical workstation. The 3DG and 3DG- MnO_2 were directly applied as the working electrode and 1.0 mol L^{-1} Na_2SO_4 was used as aqueous electrolyte. The mass loading for each electrode is typically of 1.0 mg cm^{-2} . In a three-electrode configuration, the Pt foil and the Ag/AgCl electrode were applied as count electrode and reference electrodes, respectively. The specific capacitance was calculated from the galvanostatic discharge process according to the following equation: $C = I \times \Delta t / (\Delta V \times m)$, where I is the discharge current (A), Δt is the discharge time (s), ΔV is the voltage change (V) excluding the IR drop during the discharge process, and m is the mass of the active material of MnO_2 (g) excluding the 3DG due to its negligible contribution to the capacitance, which will be discussed later. In a two-electrode system, the capacitor was configured with 3DG- MnO_2 as symmetric electrode and Celgard® 3501 membrane as separator. The specific capacitance was calculated using $C = 4 \times I \times \Delta t / (\Delta V \times m)$, where m is the total mass of the electrode. The electrochemical impedance spectroscopy (EIS) was performed with an amplitude of 5 mV at the frequency range of 0.01 to 100 kHz.

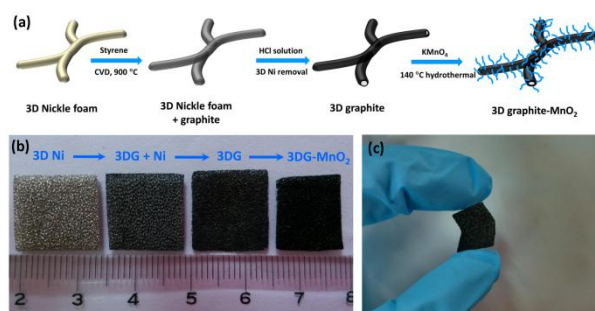


Fig. 1 Schematic illustration of the preparation procedure for MnO_2 nanoflakes grown on 3D graphite network (a), photography of the samples fabricated in each steps (b) and the obtained free-standing 3D graphite network with good flexibility (c)

Results and discussion

Fig. 1a schematically illustrates the fabrication procedures of 3DG with nickel foam as sacrificial template and styrene as the carbon precursor. Compared to the commonly used gaseous carbon precursor like methane and ethanol,^{20,24,30,33} use of styrene makes the present CVD process more safe and cost-effective. Fig. 1b shows the digital photos of samples fabricated in each steps. The color of nickel foam changes from initial shiny white into dark gray after the carbon deposition. Upon removing the nickel foam scaffold from the graphite-nickel foam composite, the macroscopic morphology of nickel foam was well retained. Moreover, the free-standing 3DG with a good mechanical flexibility was also evident from Fig. 1c. Fig. 2a displays the XRD patterns of the 3DG and graphite-nickel foam composite. The growth of the graphite on the surface of 3D nickel foam was verified by the occurrence of a diffraction peak at $2\theta = 26.52^\circ$, which can be index to the (002) diffractions of graphitic carbon. This peak become more intensive upon removing Ni foam with aqueous HCl, indicating a good crystallinity of the graphite backbone. Fig. 2b presents the typical Raman spectrum of 3DG. The high intensity of G band (1581 cm^{-1}) and an asymmetric 2D band (2730 cm^{-1}) can be clearly seen. Whereas, the usual D band which is characterized by the disordered carbon in graphene was nearly not observed. These observations agree well with the XRD patterns and reveal a high quality of the as-grown graphite.⁴⁰ The intensity ratio of 2D band to G band (I_{2D}/I_G) of 0.45, along with the 60 cm^{-1} of FWHM of 2D band indicate that the graphene layer number is about 4-6 layers in the 3DG backbone.^{41,42}

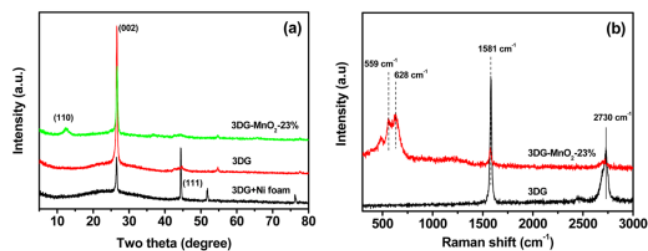


Fig. 2 Powder XRD patterns (a) and the Raman spectra (b) of 3DG and 3DG-MnO₂ composite.

The morphology of the resulting 3D graphite was examined by SEM and the representative SEM image was presented in Fig. 3a. It is clearly seen that the graphite network is composed of continuous skeleton with interconnected micrometer-sized macropore, which resembles that of the initial 3D nickel foam (Fig. S1). The identical macroscopic morphology as compared with the Ni foam template clearly demonstrates an effective replication of the CVD process. It is noteworthy that the seamlessly interconnected 3D graphite network largely minimizes the inter-sheet junctions and favors the rapid electron transport within the whole framework.^{30, 32, 36} The HRTEM image shown in Fig. 3b gives more detailed information about the graphitization of the graphite skeleton. It is seen that the skeleton is composed of graphene sheets with a thickness variation from 1.4 to 1.9 nm, corresponding to a layer number of 4–6. This observation is consistent with the result deduced from the Raman spectrum (Fig. 2b). Moreover, the selected area electron diffraction (inset in Fig.

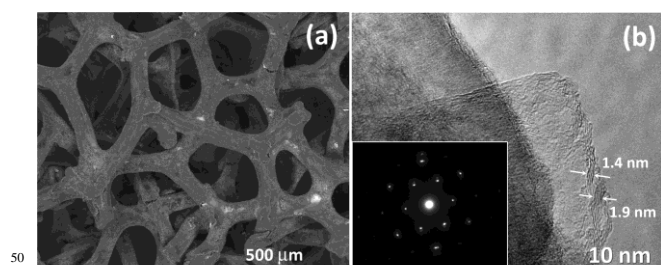


Fig. 3 SEM (a) and TEM images (b) of 3DG with inset showing the selected area electron diffraction pattern.

3b) presents the characteristic hexagonal spot patterns, further verifying the high quality of the graphite network prepared by the present CVD. The electrical conductivity of the 3DG was also measured by a four-point probe technique. A remarkably high electrical conductivity of $1.5 \times 10^3\text{ S m}^{-1}$ as compared with typical $10\text{--}500\text{ S m}^{-1}$ for most of the chemically derived graphene^{43,44} provides further evidence that the 3DG is highly crystallized.

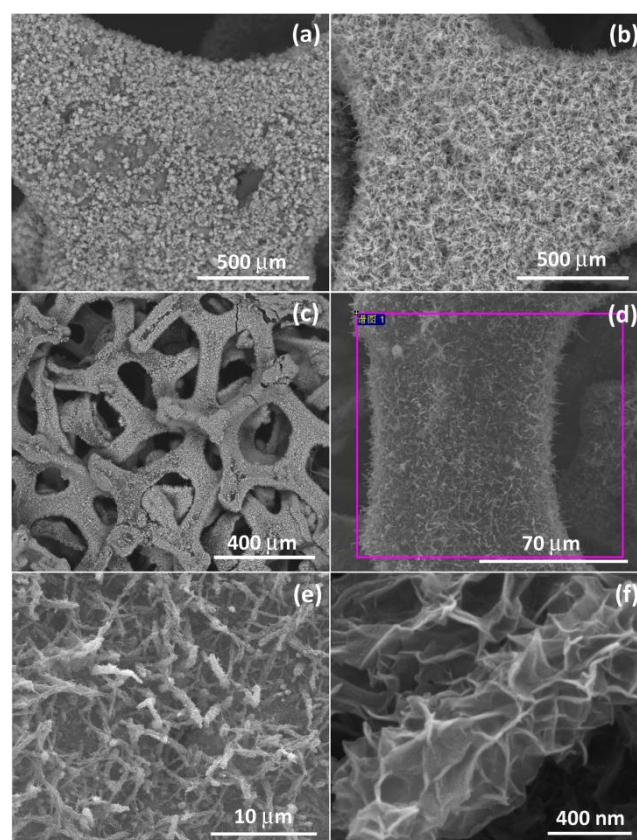


Fig. 4 SEM of 3DG-MnO₂-13% (a), 3DG-MnO₂-35% (b) and 3DG-MnO₂-23% (c, e, f) with different magnifications. (d) STEM images of 3DG-MnO₂-23%.

The 3D graphite network was used as the scaffold to grow MnO₂ nanoflakes through a hydrothermal reaction between carbonaceous materials and the aqueous KMnO₄ solution. The phase of manganese oxides in the composite was firstly identified by XRD (Fig. 2a). Apart from the strong (002) diffraction attributed to the graphite network, an additional weak peak occurring at $2\theta = 12.63^\circ$ could be indexed to the (001) reflection of birnessite-type MnO₂ (JCPDS 42-1317) with a d (001) value of 0.70 nm, which is in good consistence with the that of the layered

birnessite-type MnO_2 prepared by a sol-gel route.⁴⁵ The Raman spectrum of 3DG- MnO_2 shows two evident bands at 560 and 632 cm^{-1} (Fig. 2b). The band of 560 cm^{-1} corresponds to the Mn-O stretching vibration in the basal plane of MnO_2 sheet, whereas, the 632 cm^{-1} is related to the symmetric stretching vibration of MnO_2 groups.⁴⁶ These observations confirm the formation of birnessite-type MnO_2 as the result of stoichiometric reaction of 3D graphite network with the aqueous KMnO_4 solution.

The morphology of MnO_2 on the 3D graphite network was characterized by SEM. In spite of the MnO_2 content varying from 13% to 35%, the 3DG- MnO_2 composite remains the similar morphology to that of pristine 3DG except that its skeleton surface became coarser as the result of the growth of MnO_2 nanoflakes (Fig. 4a-c). At a low MnO_2 loading of 13%, a partial of the 3DG skeleton surface can still be visible (Fig. 4a). When the MnO_2 loading increase to over 23%, the 3DG surface was completely covered by the dense fiber-like MnO_2 (Fig. 4b and 4c). The EDX spectrum (Fig. S2) recorded in the selected area of Fig. 4d presents the element C, Mn, K and O, confirming the uniform dispersion of MnO_2 on the backbone of 3DG. A close examination shows that the MnO_2 grown on graphene network exhibit the uniform bundle-like structure (Fig. 4e). A more high-magnification SEM image shown in Fig. 4f reveals that each bundle is actually composed of a great number of ultrathin MnO_2 nanoflakes. Such a hierarchical structure is of great significance for maximizing the electrochemical redox reaction because it not only offers a large contact area for effective electrolyte penetration but also provides a shortened ion diffusion pathway, allowing for a fast migration of electrolyte ion at a very high current density.

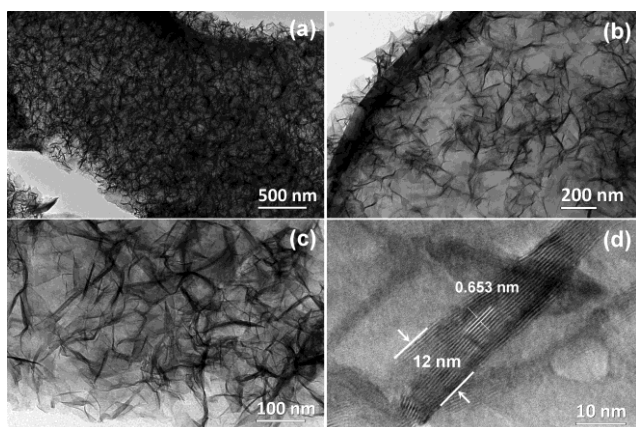


Fig. 5 TEM images of 3DG- MnO_2 -23% composite with low (a, b) and high magnification (c, d).

Fig. 5 shows the TEM images of the 3DG- MnO_2 composite. It is clearly seen that the graphite skeleton was fully surrounded by the uniform MnO_2 nanoflakes (Fig. 5a and 5b). While ultrasonic treatment was used for TEM sample preparation, the MnO_2 are still firmly connected onto the graphene skeleton without notable peeling off (Fig. 5b). Such an intimate junction indeed minimize the interfacial contact resistance between the highly conductive graphite skeleton and the pseudocapacitive MnO_2 and would greatly facilitate the electron transport at high discharge current density. The representative HRTEM images of the individual MnO_2 nanoflake shows a thickness of ~ 12 nm with a lattice spacing of 0.653 nm (Fig. 5d), corresponding to the

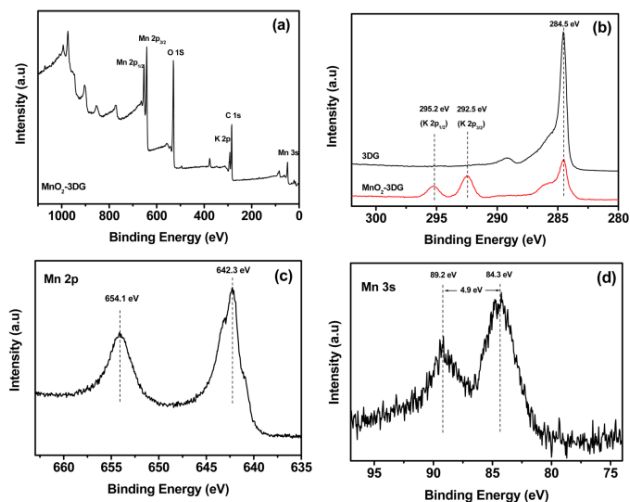


Fig. 6 XPS spectra of 3DG- MnO_2 -23% composite. (a) survey XPS, (b) C 1s XPS spectra of 3DG and 3DG- MnO_2 -23%, (c) Mn 2p and (d) Mn 3s XPS spectrum.

spacing of (110) plane of birnessite-type MnO_2 ,^{26,45} also in consistence with the result calculated from Bragg equation.

The chemical composition of 3DG- MnO_2 was characterized by XPS. The occurrence of element Mn, O, C and K is evident in the survey XPS (Fig. 6a), in accordance with the EDX result in Fig. S2. As shown in Fig. 6b, the signals of element K at binding energy of 292.5 eV ($\text{K } 2p_{3/2}$) and 295.2 eV ($\text{K } 2p_{1/2}$) can be assigned to the K^+ that occupy the interlayer space of birnessite-type MnO_2 to compensate the lower oxidation state of Mn.^{16, 45} Two characteristic peaks of Mn 2p spectrum at 654.1 and 642.3 eV correspond to the $\text{Mn } 2p_{3/2}$ and $\text{Mn } 2p_{1/2}$, respectively. According to the relation between the oxidation state of Mn and the separation of peak energy ΔE (Mn 3s),⁴⁷ the ΔE of 4.9 eV means that the average oxidation state of element Mn in 3DG- MnO_2 composite is around ~ 3.7 (Fig. 6d), showing dominant Mn^{4+} in birnessite-type MnO_2 .

The capacitive performance of 3DG and 3DG- MnO_2 electrode were evaluated by CV, galvanostatic charge-discharge and electrochemical impedance spectroscopy (EIS). Fig. 7a shows the CV behavior of 3DG electrode measured in a three-electrode system with 1.0 mol L^{-1} Na_2SO_4 as aqueous electrolyte. Even at a very high scan rate of 2 V s^{-1} , the CV of 3DG electrode still remains a quite good rectangular shape, demonstrating a high-rate electrochemical behavior as the result of fast electrostatic ion adsorption on the surface of 3DG electrode. After growth of 13% MnO_2 , the composite electrode exhibits a dramatically increased current response as compared with that of 3DG electrode, highlighting the significant role of MnO_2 nanoflakes in dramatically improving the overall capacitance of composite electrode (Fig. 7b). The much small integrated area of 3DG electrode implies a quite low ion-accessible surface area which is presumably related to the hydrophobic surface nature of 3DG electrode. Fig. 7c shows the CV profiles of 3DG- MnO_2 -13% electrode at various scan rates. The nearly linear increase of current density with the scan rate up to 300 mV s^{-1} indicates an ideal capacitive behavior (Fig. S3). The superior electrochemical performance clearly reveals the crucial role of the highly

Cite this: DOI: 10.1039/c0xx00000x

www.rsc.org/xxxxxx

ARTICLE TYPE

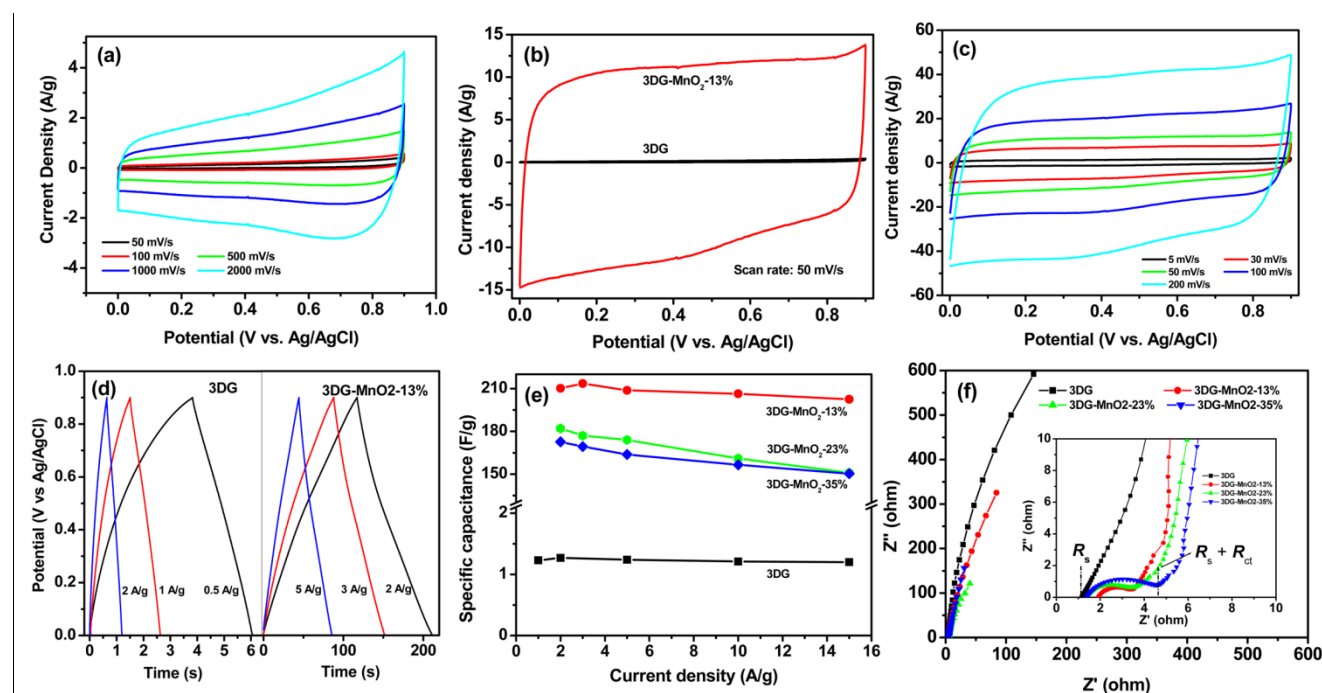


Fig. 7 CV profiles of 3DG at different scan rates (a), and CV curve of 3DG and 3DG-MnO₂-13% composite at a scan rate of 50 mV/s (b). The CV of 3DG-MnO₂-13% at various scan rates (c). The comparative galvanostatic charge-discharge curves of 3DG and 3DG-MnO₂-13% composite electrode (d). The capacitance retention (e) and Nyquist plots (f) of 3DG and 3DG-MnO₂ composite electrode with inset showing the plots in the high-frequency region.

5 conductive 3DG skeleton which significantly enhance the fast ion and electron migration throughout the 3DG-MnO₂ composite electrode.

The galvanostatic charge-discharge profile of 3DG and 3DG-MnO₂ was compared in Fig. 7d. The nearly symmetric charge-discharge curves of 3DG electrode at different current densities is characterized by a double-layer charge storage mechanism. While the triangular profile of 3DG-MnO₂-13% reveals the reversible pseudocapacitive reaction between Na⁺ and MnO₂ electrode.⁴⁸ No distinct IR drop was observed for the composite electrode even at a very high current density of 5.0 A g⁻¹, implying a rather low equivalent series resistance (ESR) as the result of short ion diffusion pathway and excellent electrical conductivity of the underlying 3D skeleton. The high-rate performance of the composite electrode was also evidenced by increasing the MnO₂ loading from 13%, 23% to 35%. As shown in Fig. 7e, the specific capacitance of the composite electrode reach 210, 182 and 173 F g⁻¹ at 2.0 A g⁻¹ when MnO₂ loading is 13%, 23% to 35%, respectively. Considering the typical mass loading of 1.0 mg cm⁻¹ for each electrode, their corresponding area capacitances were calculated to be 0.21, 0.18 and 0.17 F cm⁻², respectively. The much lower area capacitance as compared with 1.42 F cm⁻¹ of previous 3D graphen/MnO₂ composite electrode²⁴ might be due to the low mass loading of our samples (1.0 vs 9.8 mg cm⁻¹). Nevertheless, the capacitances remain a high value of 203, 151 and 150 F g⁻¹ even at a high current density of 15 A g⁻¹,

corresponding to a capacitance retention of 97%, 83% and 87% for MnO₂ loading of 13, 23 and 35%, respectively. While the specific capacitance of composite electrode is somewhat lower than that of previous results,^{20, 49-51} the capacitance retention of MnO₂-RGO electrode is significantly higher than that of MnO₂-RGO composite electrodes prepared by an electrostatic assembly or the physical combining method, such as 60-70% of birnessite-type MnO₂ dispersed on functionalized RGO electrode,^{27, 28, 52} 54% of MnO₂-CNT-graphene electrode (from 0.2 to 5.0 A/g),²⁶ 50% of CNTs/MnO₂ thin film electrode (from 10 to 1000 mV/s),⁵³ 45% of graphene/MnO₂/CNTs film (from 10 to 500 mV/s),⁵⁴ and 30% of MnO₂ deposited on highly conductive porous Au electrode (from 0.3 to 20 A/g).¹² The remarkable high-rate performance of the composite electrode is directly related to the highly conductive 3DG network and the intimate junction between MnO₂ nanoflakes and the backbone surface of the interconnected 3DG skeleton. Meanwhile, the individual MnO₂ with ultrathin nanoflakes also greatly shorten the ion diffusion pathway for rapid access of Na⁺ to the electrode surface. These unique properties make 3DG-MnO₂ composite one of the promising candidates for high-rate supercapacitor electrode.

The electrochemical impedance spectroscopy of 3DG and the 3DG-MnO₂ composite electrode was measured at the frequency range from 0.01 Hz to 100 kHz and the typical Nyquist plots were shown in Fig. 7f. In the low frequency range, 3DG electrode exhibits nearly a vertical curve along the imaginary axis, in

accordance with its charge storage through an ion adsorption mechanism. Whereas, the 3DG-MnO₂ electrode displays a more inclined profile, an indicative of significant contribution from surface Faradic redox reaction. In the high frequency range, neither the semicircle nor the Warburg portion was observed for 3DG electrode (inset in Fig. 7f), suggesting an extremely low ESR due to the rapid ion and electron transport.⁵⁵ In contrast, for 3DG-MnO₂ composite electrode, a semicircle intercepts the real axis at R_s (solution resistance) in the very high-frequency, and $R_s + R_{ct}$ (charge transfer resistance) in the high-frequency (inset in Fig. 7f). The progressive increase in semicircle with the MnO₂ loading reflects a slight decrease of the charge transfer rate due to the incorporation of the poorly conductive MnO₂ (10^{-5} to 10^{-6} S cm⁻¹).¹⁶ Considering the MnO₂ loading varying from 13% to 35%, the increase of R_{ct} from 3.5 to 5.0 Ω is not a prominent one.

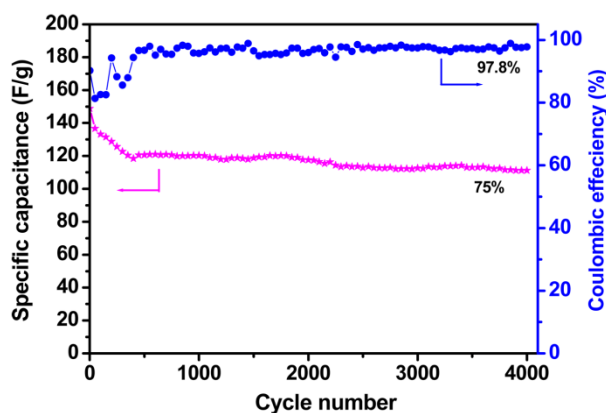


Fig. 8 Cycle performance and Coulombic efficiency of 3DG-MnO₂-23% composite electrode at a current density of 4.0 A g⁻¹ in 1.0 mol L⁻¹ aqueous Na₂SO₄ solution

To test the long-term cycling performance, the composite electrode with a high MnO₂ loading of 23% was measured by a continuous galvanostatic charge-discharge at constant current density of 4.0 A g⁻¹ (Fig. 8). The 3DG-MnO₂ electrode shows slight decrease in specific capacitance at initial 400 cycles and then remains quite stable capacitance value in the subsequent 3600 cycles. It has been proposed that electrode dissolution during the cycling might be one of crucial reasons for the capacitance decay of MnO₂-based electrode.⁵⁶ In our cycling measurement, we noted a small amount of MnO₂ was dissolved as the electrolyte turned from initial colorless into pale yellow. A plausible reason might be that the MnO₂ bundles protruding out from the 3DG is vulnerable to the continuous insertion/deinsertion of Na⁺ into and out of the MnO₂ nanoflakes during the charging/discharging process. Nevertheless, the 3DG-MnO₂ electrode preserved 75% of its initial capacitance after 4000 cycles of galvanostatic charge-discharge. The Coulombic efficiency, an indicative of the reversibility of electrode materials, however, remains a quite high value of 97.8%. This result reveals a highly reversible pseudocapacitance reaction between Na⁺ and MnO₂ nanoflakes. The symmetric charge-discharge curves of the last 10 cycles (Fig. S5) also support this electrochemical stability.

A two-electrode capacitor with symmetric 3DG-MnO₂-13% electrode was configured and its capacitive performance was also tested at a voltage window of 0-0.8 V. The CV shows a quasi-

rectangular profile over a wide range of scan rates (Fig. S5a), demonstrating its excellent capacitive behavior. The galvanostatic charge-discharge also displays symmetric profile at different current densities (Fig. S5b). The specific capacitance based on the total mass of two electrodes was measured to be 36 F g⁻¹ at constant current density of 0.5 A g⁻¹, corresponding to 134 F g⁻¹ for a single electrode when multiplying a coefficient of 4. This observation follow the best practice method as described by Ruoff and his coworkers.⁵⁷

Conclusions

We have successfully prepared the 3D graphite network by a chemical vapor deposition with 3D Ni foam as sacrificial template and styrene as carbon precursor. The seamlessly interconnected 3D network with high graphitization make the 3DG an ideal scaffold to accommodate various pseudocapacitive components. A hydrothermal reaction between 3DG and aqueous KMnO₄ yields a hierarchical nanostructure with MnO₂ nanoflakes that were uniformly deposited on the surface of 3DG backbone. The highly conductive 3DG serves as an excellent network to greatly enhance the electron and ion transport, while the MnO₂ nanoflakes emanating from 3DG backbone offer a large electrochemically active surface area and a shortened diffusion pathway for effective electrolyte penetration. Consequently, the 3DG-MnO₂ electrode electrode delivery a specific capacitance of 210 F g⁻¹ as compared with 1.3 F g⁻¹ of 3DG electrode at 2.0 A g⁻¹ and remained an remarkably high-rate performance. Moreover, a reasonable cycling stability and an outstanding Coulombic efficiency were simultaneously achieved after 4000 cycles of consecutive charge-discharge, making the 3DG-MnO₂ composite one of promising electrode for electrochemical energy storage. The cost-effective CVD method for preparing 3D graphite network would also open up new opportunities to process 3D graphite-based functional materials for wide applications in biosensor, nanoelectronics, solar cells and so on.

Acknowledgements

This work was financially supported by the National Nature Science Foundations of China (Grant No. 21373134, 51172137), Fundamental Research Funds for the Central Universities (Grant No: GK201403005, GK201101003, GK201301002), the foundation of returned overseas scholar, MOE, and the Program for Key Science & Technology Innovation Team (2012KCT-21) and Nature Science Foundation of Shaanxi Province (2013JM2001).

Notes and references

- ^a School of Materials Science and Engineering, Shaanxi Normal University, 620 West Chang'an Street, Xi'an, Shaanxi, 710119, China, Fax: 86-29-81530702; Tel: 86-29-81530810; E-mail: zblei@snnu.edu.cn
^b School of Chemistry and Chemical Engineering, Shaanxi Normal University, 620 West Chang'an Street, Xi'an, Shaanxi, 710119, China, Email: weill@snnu.edu.cn

Electronic Supplementary Information (ESI) available: The SEM images of 3D Ni foam, EDX spectrum of MnO₂-3DG-23%, the dependence of discharged current density on the scan rate for 3DG-MnO₂-13% electrode, the last 10 cycles of galvanostatic charge-discharge curves of 3DG-MnO₂-23%, and the capacitive performance of two-

- electrode capacitor with 3DG-MnO₂-13% as symmetric electrode. See DOI: 10.1039/b000000x/
- 1 P. Simon and Y. Gogotsi, *Acc. Chem. Res.*, 2013, **46**, 1094-1103.
 - 2 H. Jiang, P. S. Lee and C. Li, *Energy Environ. Sci.*, 2013, **6**, 41-53.
 - 3 L. Jiang and Z. Fan, *Nanoscale*, 2014, **6**, 1922-1945.
 - 4 M. Beidaghi and Y. Gogotsi, *Energy Environ. Sci.*, 2014, **7**, 867-884.
 - 5 H. Ji, X. Zhao, Z. Qiao, J. Jung, Y. Zhu, Y. Lu, L. L. Zhang, A. H. MacDonald and R. S. Ruoff, *Nat. Commun.*, 2014, **5**:3317.
 - 6 J. R. Miller and P. Simon, *Science*, 2008, **321**, 651-652.
 - 7 J. Chmiola, C. Largeot, P. L. Taberna, P. Simon and Y. Gogotsi, *Science*, 2010, **328**, 480-483.
 - 8 L. L. Zhang, Y. Gu and X. S. Zhao, *J. Mater. Chem. A*, 2013, **1**, 9395-9408.
 - 9 P. Simon and Y. Gogotsi, *Nat. Mater.*, 2008, **7**, 845-854.
 - 10 W. F. Wei, X. W. Cui, W. X. Chen and D. G. Ivey, *Chem. Soc. Rev.*, 2011, **40**, 1697-1721.
 - 11 A. Sumbaja, C. Y. Foo, X. Wang and P. S. Lee, *Adv. Mater.*, 2013, **25**, 2809-2815.
 - 12 X. Lang, A. Hirata, T. Fujita and M. Chen, *Nat Nano*, 2011, **6**, 232-236.
 - 13 Y. Zhang, M. Ma, J. Yang, W. Huang and X. Dong, *RSC Advances*, 2014, **4**, 8466-8471.
 - 14 L. Athouël, F. Moser, R. Dugas, O. Crosnier, D. Bédanger and T. Brousse, *J. Phys. Chem. C*, 2008, **112**, 7270-7277.
 - 15 S.-L. Kuo and N.-L. Wu, *J. Electrochem. Soc.*, 2006, **153**, A1317-A1324.
 - 16 Z. Lei, J. Zhang and X. S. Zhao, *J. Mater. Chem.*, 2012, **22**, 153-160.
 - 17 J. Liu, J. Jiang, C. Cheng, H. Li, J. Zhang, H. Gong and H. J. Fan, *Adv. Mater.*, 2011, **23**, 2076-2081.
 - 18 X. Zhao, L. Zhang, S. Murali, M. D. Stoller, Q. Zhang, Y. Zhu and R. S. Ruoff, *ACS Nano*, 2012, **6**, 5404-5412.
 - 19 H. Jiang, J. Ma and C. Li, *Adv. Mater.*, 2012, **24**, 4197-4202.
 - 20 X. Dong, X. Wang, J. Wang, H. Song, X. Li, L. Wang, M. B. Chan-Park, C. M. Li and P. Chen, *Carbon*, 2012, **50**, 4865-4870.
 - 21 C. Xu, B. Xu, Y. Gu, Z. Xiong, J. Sun and X. S. Zhao, *Energy Environ. Sci.*, 2013, **6**, 1388-1414.
 - 22 C. Wu, S. Deng, H. Wang, Y. Sun, J. Liu and H. Yan, *ACS Appl. Mater. Interfaces*, 2014, **6**, 1106-1112.
 - 23 J. Ji, L. L. Zhang, H. Ji, Y. Li, X. Zhao, X. Bai, X. Fan, F. Zhang and R. S. Ruoff, *ACS Nano*, 2013, **7**, 6237-6243.
 - 24 Y. He, W. Chen, X. Li, Z. Zhang, J. Fu, C. Zhao and E. Xie, *ACS Nano*, 2013, **7**, 174-182.
 - 25 Y. Wang, X. Yang, L. Qiu and D. Li, *Energy Environ. Sci.*, 2013, **6**, 477-481.
 - 26 Z. B. Lei, F. Shi and L. Lu, *ACS Appl. Mater. Interfaces*, 2012, **4**, 1058-1064.
 - 27 J. Zhang and X. S. Zhao, *Carbon*, 2013, **52**, 1-9.
 - 28 J. Zhu and J. He, *ACS Appl. Mater. Interfaces*, 2012, **4**, 1770-1776.
 - 29 H. Chen, S. Zhou, M. Chen and L. Wu, *J. Mater. Chem.*, 2012, **22**, 25207-25216.
 - 30 Z. Chen, W. Ren, L. Gao, B. Liu, S. Pei and H.-M. Cheng, *Nat. Mater.*, 2011, **10**, 424-428.
 - 31 B. G. Choi, M. Yang, W. H. Hong, J. W. Choi and Y. S. Huh, *ACS Nano*, 2012, **6**, 4020-4028.
 - 32 Z. Yan, L. Ma, Y. Zhu, I. Lahiri, M. G. Hahm, Z. Liu, S. Yang, C. Xiang, W. Lu, Z. Peng, Z. Sun, C. Kittrell, J. Lou, W. Choi, P. M. Ajayan and J. M. Tour, *ACS Nano*, 2013, **7**, 58-64.
 - 33 X. Cao, Y. Shi, W. Shi, G. Lu, X. Huang, Q. Yan, Q. Zhang and H. Zhang, *Small*, 2011, **7**, 3163-3168.
 - 34 M. F. El-Kady, V. Strong, S. Dubin and R. B. Kaner, *Science*, 2012, **335**, 1326-1330.
 - 35 J. H. Lee, N. Park, B. G. Kim, D. S. Jung, K. Im, J. Hur and J. W. Choi, *ACS Nano*, 2013, **7**, 9366-9374.
 - 36 X.-C. Dong, H. Xu, X.-W. Wang, Y.-X. Huang, M. B. Chan-Park, H. Zhang, L.-H. Wang, W. Huang and P. Chen, *ACS Nano*, 2012, **6**, 3206-3213.
 - 37 X. Cao, Z. Yin and H. Zhang, *Energy Environ. Sci.*, 2014, **7**, 1850-1865.
 - 38 S. Han, D. Wu, S. Li, F. Zhang and X. Feng, *Adv. Mater.*, 2014, **26**, 849-864.
 - 39 X. Jin, W. Zhou, S. Zhang and G. Z. Chen, *Small*, 2007, **3**, 1513-1517.
 - 40 H. Ji, L. Zhang, M. T. Pettes, H. Li, S. Chen, L. Shi, R. Piner and R. S. Ruoff, *Nano Lett.*, 2012, **12**, 2446-2451.
 - 41 A. C. Ferrari, J. C. Meyer, V. Scardaci, C. Casiraghi, M. Lazzeri, F. Mauri, S. Piscanec, D. Jiang, K. S. Novoselov, S. Roth and A. K. Geim, *Phys. Rev. Lett.*, 2006, **97**, 187401.
 - 42 Y. Hao, Y. Wang, L. Wang, Z. Ni, Z. Wang, R. Wang, C. K. Koo, Z. Shen and J. T. L. Thong, *Small*, 2010, **6**, 195-200.
 - 43 D. C. Luo, G. X. Zhang, J. F. Liu and X. M. Sun, *J. Phys. Chem. C*, 2011, **115**, 11327-11335.
 - 44 Z. Lei, L. Lu and X. S. Zhao, *Energy Environ. Sci.*, 2012, **5**, 6391-6399.
 - 45 S. Ching, D. J. Petrovay, M. L. Jorgensen and S. L. Suib, *Inorg. Chem.*, 1997, **36**, 883-890.
 - 46 S. B. Ma, Y. H. Lee, K. Y. Ahn, C. M. Kim, K. H. Oh and K. B. Kim, *J. Electrochem. Soc.*, 2006, **153**, C27-C32.
 - 47 M. Toupin, T. Brousse and D. Bédanger, *Chem. Mater.*, 2002, **14**, 3946-3952.
 - 48 M. Toupin, T. Brousse and D. Bédanger, *Chem. Mater.*, 2004, **16**, 3184-3190.
 - 49 L. Mao, K. Zhang, H. S. On Chan and J. Wu, *J. Mater. Chem.*, 2012, **22**, 1845-1851.
 - 50 S. Wu, W. Chen and L. Yan, *J. Mater. Chem. A*, 2014, **2**, 2765-2772.
 - 51 U. M. Patil, J. S. Sohn, S. B. Kulkarni, H. G. Park, Y. Jung, K. V. Gurav, J. H. Kim and S. C. Jun, *Mater. Lett.*, 2014, **119**, 135-139.
 - 52 J. T. Zhang, J. W. Jiang and X. S. Zhao, *J. Phys. Chem. C*, 2011, **115**, 6448-6454.
 - 53 S. W. Lee, J. Kim, S. Chen, P. T. Hammond and Y. Shao-Horn, *ACS Nano*, 2010, **4**, 3889-3896.
 - 54 Y. Cheng, S. Lu, H. Zhang, C. V. Varanasi and J. Liu, *Nano Lett.*, 2012, **12**, 4206-4211.
 - 55 L. L. Zhang, X. Zhao, M. D. Stoller, Y. Zhu, H. Ji, S. Murali, Y. Wu, S. Perales, B. Clevenger and R. S. Ruoff, *Nano Lett.*, 2012, **12**, 1806-1812.
 - 56 Belanger D, T.Brousse and W. L. J., *Electrochem. Soc. Interface*, 2008, 49-52.
 - 57 M. D. Stoller and R. S. Ruoff, *Energy Environ. Sci.*, 2010, **3**, 1294-1301.